Nanoscale

COMMUNICATION

View Article Online
View Journal | View Issue

Cite this: *Nanoscale*, 2016, **8**, 19211

Received 11th October 2016,
Accepted 30th October 2016

DOI: 10.1039/c6nr07977f

www.rsc.org/nanoscale

Interlayer thermal conductance within a phosphorene and graphene bilayer

Yang Hong,[a] Jingchao Zhang*[b] and Xiao Cheng Zeng*[a]

Monolayer graphene possesses unusual thermal properties, and is often considered as a prototype system for the study of thermal physics of low-dimensional electronic/thermal materials, despite the absence of a direct bandgap. Another two-dimensional (2D) atomic layered material, phosphorene, is a natural p-type semiconductor and it has attracted growing interest in recent years. When a graphene monolayer is overlaid on phosphorene, the hybrid van der Waals (vdW) bilayer becomes a potential candidate for high-performance thermal/electronic applications, owing to the combination of the direct-bandgap properties of phosphorene with the exceptional thermal properties of graphene. In this work, the interlayer thermal conductance at the phosphorene/graphene interface is systematically investigated using classical molecular dynamics (MD) simulation. The transient pump–probe heating method is employed to compute the interfacial thermal resistance (*R*) of the bilayer. The predicted *R* value at the phosphorene/graphene interface is 8.41 × 10^{-8} K m^2 W^{-1} at room temperature. Different external and internal conditions, *i.e.*, temperature, contact pressure, vacancy defect, and chemical functionalization, can all effectively reduce *R* at the interface. Numerical results of *R* reduction as a function of temperature, interfacial coupling strength, defect ratio, or hydrogen coverage are reported with the most *R* reduction amounting to 56.5%, 70.4%, 34.8% and 84.5%, respectively.

1. Introduction

The miniaturization of modern electronic devices demands the urgent development of high-performance and cost-effective thermal pathways at the nanoscale. The emergence of high thermal conductivity (κ) two dimensional (2D) monolayer structures, such as graphene, phosphorene, hexagonal boron nitride and molybdenum disulfide, has attracted enormous attention in recent years. Among these 2D materials, graphene stands out by itself with novel thermal properties[1–3] and superb thermal conductivities of 3000–5000 W m^{-1} K^{-1} at room temperature.[4] It is considered as the most promising candidate for resolving the thermal dissipation problems in nanodevices.[5] However, the absence of a direct electronic bandgap limits its applications in nanodevices such as field effect transistors (FETs).[6–8] Therefore, considerable efforts have been devoted to seeking other 2D materials with desired and tunable bandgaps as well as inherently good thermal properties. The 2D transition-metal dichalcogenides (TMDCs) are a possibility to fill the role. Another good candidate is the 2D phosphorene which has been successfully peeled off from black bulk phosphorus. Phosphorene also possesses novel structural and electronic properties, *e.g.*, layer-dependent direct bandgaps (1.51 eV to 0.59 eV with layer numbers from 1 to 5), high electron/hole mobility (up to 1000 cm^2 V^{-1} s^{-1}), as well as high current modulation (up to 10^5), which can be exploited for nanoelectronic applications.[9–13] Compared to other 2D materials such as TMDCs and silicene, phosphorene has a relatively high thermal conductivity (κ) of 63.6 W m^{-1} K^{-1} and 110.7 W m^{-1} K^{-1} in armchair and zigzag directions, respectively. However, its κ value is still an order of magnitude smaller than that of suspended graphene.[10]

The advancement in the fabrication of 2D van der Waals (vdW) heterostructures provides a way to take advantage of the best properties of different 2D materials together. Apart from directly assembling individual monolayers, the physical epitaxy and chemical vapor deposition (CVD) can offer even faster large-area growth methods.[14] Lately, it has been shown that stacking a graphene/phosphorene vdW bilayer can preserve their properties in the ultimate heterostructure.[15] The relative position of phosphorene's band structure with respect to graphene's can be tuned *via* a vertical external electric field. Moreover, by exploring the electric field dependent band structures and optical properties of the graphene/phosphorene bilayer system, Hashmi *et al.*[16] demonstrate that the bilayer heterostructure can be applied to a high-speed device although the optical anisotropy in the bilayer structure for in-plane

[a]*Department of Chemistry, University of Nebraska-Lincoln, Lincoln, NE 68588, USA. E-mail: xzeng1@unl.edu*
[b]*Holland Computing Center, University of Nebraska-Lincoln, Lincoln, NE, 68588, USA. E-mail: zhang@unl.edu*

electric field polarization has disappeared. Due to the presence of the lone-pair state, monolayer phosphorene can be corrugated when in contact with common metal electrodes, which may degrade its performance. Conversely, graphene has excellent structural integrity with both metal electrodes and phosphorene due to its atomically smooth surface. Thus, graphene can serve as a perfect interfacial material between the phosphorene and metal electrodes.[17] To our best knowledge, the thermal conductance of graphene/phosphorene has not been investigated yet. In this work, the interfacial thermal transport at a graphene/phosphorene bilayer heterostructure is systematically investigated using classical molecular dynamics (MD) simulations. To facilitate the thermal dissipation at the out-of-plane direction, several modulators, *i.e.*, system temperature, contact pressure, surface defect and chemical functionalization, are considered and their effects on the reduction of thermal contact resistance (R) are significant. In the following sections, the system construction and the approach for R computation are explained. Detailed phonon power spectrum analyses are conducted for in-depth discussions.

2. Simulation and numerical methods

All simulations are performed using the large-scale atomic/molecular massively parallel simulator (LAMMPS) program.[18] The C–C interactions within graphene are described by the second generation of Brenner's potential, *i.e.*, reactive empirical bond-order (REBO).[19] The P–P interactions are modelled by a Stillinger–Weber (SW) potential,[20] which has been previously tested in the studies of phosphorene's mechanical, thermal and optical properties.[21–23] Coupling between graphene and phosphorene is described by the 12-6 Lennard-Jones potential, which can be expressed as

$$V(r) = 4\chi\varepsilon\left[\left(\frac{\sigma}{r}\right)^{12} - \left(\frac{\sigma}{r}\right)^{6}\right], \quad (1)$$

where σ is the atomic length parameter; ε is the energy parameter; and r is the interatomic distance. Parameter χ is used to adjust the coupling strength. The LJ parameters are taken from the universal force field (UFF),[24] where ε_{C-P} = 7.771 meV, σ_{C-P} = 3.560 Å, ε_{H-P} = 5.030 meV and σ_{H-P} = 3.082 Å. To eliminate the size effects in lateral directions, periodic boundary conditions are applied to the in-plane x and y directions. Free-boundary conditions are used in the out-of-plane z direction to allow full relaxation of the heterostructure during equilibrium simulation. Lateral dimensions of the heterostructure are 11.8 × 12.2 ($x \times y$) nm^2. The atomic configuration of the system is shown in Fig. 1. The time step in the MD simulations is 0.5 fs (1 fs = 10^{-15} s).

The most popular MD method for Kapitza resistance characterization at bulk structure interfaces is the steady-state non-equilibrium molecular dynamics (NEMD). This approach has been widely used in previous numerical studies.[25–27] During the NEMD heating/cooling process, thermal energies are directly imposed on the heat reservoirs, making temperature measurements inaccurate near those areas. Therefore, for bilayer structures, the NEMD method cannot be used for interfacial thermal resistance characterization. In this work, a transient heating technique, which mimics the experimental pump–probe approach,[28] is applied to compute the R values between graphene/phosphorene. After the system reaches the steady state at a given temperature, an ultrafast 50 fs thermal impulse is imposed on the graphene layer. In the following thermal relaxation process, temperature evolution in both graphene and phosphorene is recorded. The total energy of the graphene system is outputted at every time step and averaged every 100 steps to suppress data noise. The thermal resistance R can be calculated by using the equation

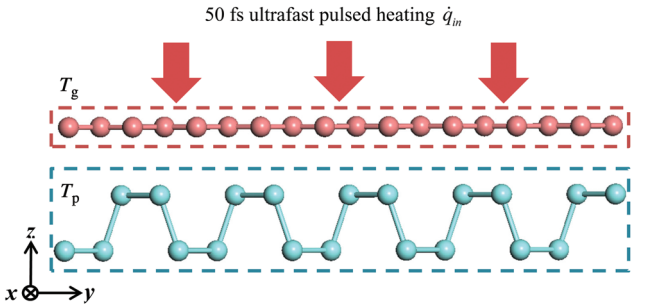

Fig. 1 Atomic configuration of the phosphorene–graphene bilayer heterostructure. An ultrafast heat impulse is introduced into the graphene monolayer for computing the interfacial thermal resistance.

$$\frac{\partial E_t}{\partial t} = \frac{A\cdot(T_p - T_g)}{R}, \quad (2)$$

where A is the interfacial area; T_g and T_p are the temperatures of graphene and phosphorene respectively; E_t is the energy of graphene at time t. This approach has been successfully applied to compute the interfacial properties of various heterostructures such as graphene/silicon,[29] graphene/copper[30] and graphene/6H-SiC.[31] Compared to the traditional NEMD method which requires a relatively long computation time to let the system reach the steady-state, the transient technique can accurately predict thermal resistance over a time scale of ~10^2 ps.

3. Results and discussion

To characterize the interfacial thermal resistance within the bilayer structure, the system is initially placed into a canonical ensemble (NVT) for 600 ps at temperature 300 K and then moved to a micro-canonical ensemble (NVE) for another 400 ps to reach thermal equilibrium. Temperature controls are applied to graphene and phosphorene monolayers separately to avoid internal temperature differences. Compared to the traditional NEMD method, this transient technique can characterize the interfacial thermal resistance in ultrathin bilayer heterostructures with less computational time. However, in order to reach stable and smooth energy and temperature evolution profiles in graphene and phosphorene, a relatively large

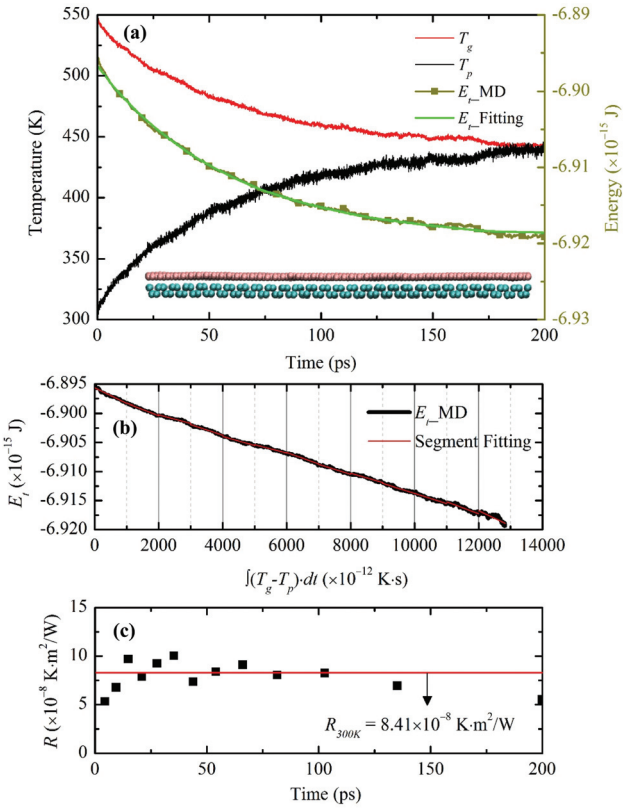

Fig. 2 (a) Temperature evolution of the individual graphene, phosphorene monolayer, and the total energy change of the graphene monolayer after introducing the thermal impulse. Atomic configuration of the heterostructure in the stable state is shown in the inset. (b) Relationship between the total energy of graphene and the temperature difference ($T_g - T_p$) integration with time. (c) Segment interfacial thermal resistance values obtained in (b).

temperature difference is required; otherwise the fitting process is subjected to temperature fluctuations and data noise. We have examined various thermal pulse intensities and found that $\dot{q} = 8 \times 10^{12}$ W m^{-2} is a good fit for the thermal resistance calculations. After the system reaches the steady state, a heat flux $\dot{q}$ of 8×10^{12} W m^{-2} is added to the graphene monolayer for 50 fs. The temperature of graphene increases to ~550 K after excitation, while the temperature of phosphorene remains at 300 K. The values of E_t, T_g and T_p are recorded in the following 200 ps relaxation process. The energy decay data are fitted in Fig. 2(a) based on the integral form of eqn (2), $E_t = E_0 + (A/R)\cdot\int_0^t (T_p - T_g)dt$, where E_0 is the initial energy. The computed interfacial thermal resistance at 300 K is 8.41 × 10^{-8} K m^2 W^{-1}, which is in the same order of magnitude as other vdW bilayer structures.[32–34] A summary of thermal resistances within common 2D material interfaces is presented in Table 1. From these data, we can conclude that R between graphene and phosphorene is higher than that between graphene and metal/polymer substrates, but is lower than graphene/silicene, graphene/*h*-BN and graphene/MoS_2 bilayer structures. The temporal evolution of R is shown in Fig. 2(b). Since the energy decay is driven by the temperature difference ΔT = ($T_g - T_p$) as shown in Fig. 2(a), the phosphorene energy changes against $\int \Delta T dt$ are plotted. It is seen that the E_t profile has a linear relationship with $\int \Delta T dt$. The E_t profile is divided into many segments as shown in Fig. 2(b). For each segment (t_1 to t_2), R can be treated as a constant, and can be determined by a linear fitting of the curve. The fitted slope equals A/R, and can be used to determine R. As presented in Fig. 2(c), the calculated instant R values vary slightly around the overall fitting results, indicating that the thermal resistance is constant during the transient process.

Table 1 A summary of the interfacial thermal resistances of popular 2D material interfaces, computed from classical MD simulations

References	Materials	Temperature (K)	R ($\times10^{-8}$ K m^2 W^{-1})
Zhang *et al.*[29]	Graphene/Si	300	3.1–4.9
Li *et al.*[52]	Graphene/SiC	300	0.091–5.6
Wang *et al.*[53]	Graphene/SiC	300–600	~1.03–1.75
Hong *et al.*[30]	Graphene/copper	300	2.1–3.6
Chang *et al.*[54]	Graphene/copper/nickel	230–430	~0.2–0.83
Luo *et al.*[55]	Graphene/polymer	298	~1.7
Liu *et al.*[32]	Graphene/silicene	200–700	~4.2–16.8
Zhang *et al.*[34]	Graphene/*h*-BN	200–700	9.04–29.6
Liu *et al.*[33]	Graphene/MoS_2	200–500	~8.3–25
Park *et al.*[56]	Graphene/CNT	10–600	~0.018–0.045
Wei *et al.*[57]	Graphene/graphene	400–1200	~0.021–0.025
Zhang *et al.*[58]	Silicene/Si/SiO_2	100–400	1.19–2.49

To have a better understanding of the interfacial thermal resistance of the heterostructure, the phonon density of states (PDOS) for both graphene and phosphorene are computed. The PDOS can be calculated by taking the Fourier transform of the velocity autocorrelation function (VACF)

$$G(\omega) = \frac{1}{\sqrt{2\pi}}\int_{-\infty}^{\infty} Z(t)e^{i\omega t}dt, \quad (3)$$

where $Z(t) = \langle\nu(0)\cdot\nu(t)\rangle/\langle\nu(0)\cdot\nu(0)\rangle$. A higher value of PDOS means that a phonon occupies more states with frequency ω, while zero PDOS means no phonon with frequency ω exists in the system. The phonon-power-spectrum analysis provides a quantitative way to assess the power carried by phonons in a system. The overall PDOS of graphene and phosphorene are depicted in Fig. 3(a). Due to the intrinsic anisotropic phonon properties of graphene, the decomposed PDOS in lateral and out-of-plane directions are calculated separately and the results are shown in Fig. 3(b) and (c). Thermal resistance is caused by the PDOS mismatch in graphene and phosphorene. Also, unlike graphene, the PDOS of phosphorene are isotropic in all directions and only appear in low frequency regions, which is the reason why phosphorene's thermal conductivity is lower than that of graphene.[10]

3.1 Effects of temperature and contact pressure

Thermal interface materials embedded in FETs or other nanodevices are often placed under different working temperatures. The accumulation of thermal energies in these confined spaces could lead to possible structural failures. Besides, the

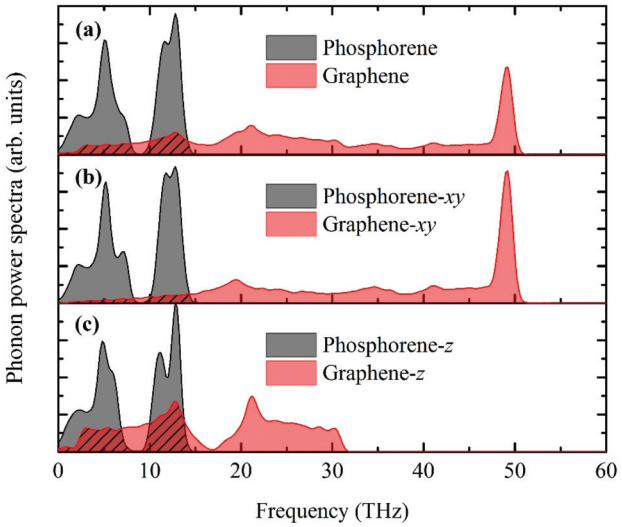

Fig. 3 Phonon-power spectra of phosphorene and graphene. (a), (b), (c) denote the overall, lateral *xy* directions, and out-of-plane *z* direction PDOS, respectively. Integration area of each profile is normalized to unity for comparison.

condensed arrangement of thermal interface materials in layered structures can cause contact pressure variations and then affect the thermal transport efficiency. Thus, to effectively reduce the thermal contact resistance between graphene and phosphorene, the effects of temperature and contact pressure on R are investigated.

To be consistent with previous computations, the system configuration and simulation setup remain unchanged. Initial equilibrium temperatures varied from 50 K to 350 K. Coupling strength χ is set to 0.5, 1.0 and 2.0 for each temperature value. Five independent simulations are performed for each case to obtain an accurate statistical average of R, as presented in Fig. 4. It is seen that the predicted R values decrease monotonically with temperature. For the $\chi = 1.0$ case, R is reduced by 56.5% from 17.34×10^{-8} K m^2 W^{-1} to 7.55×10^{-8} K m^2 W^{-1}. As the temperature increases, more phonons with a higher frequency become active in both graphene and phosphorene, which results in higher phonon populations and directly facilitates the thermal transport across the vdW interface. Besides, the more intensive three-phonon scattering at higher temperatures can scatter the high frequency phonons within graphene into various low frequency branches, leading to the higher phonon transmission coefficients and enhanced phonon couplings between graphene and phosphorene. The heat capacities of phosphorene and graphene are functions of temperature and can increase with temperature since more phonon modes would be excited, and as a result, would lead to enhanced interfacial thermal conductance and reduced thermal resistance. In this work, the heat capacities are not directly involved in the thermal resistance calculations since R is determined from temperature and energy correlations. Aside from the heat capacity effects, another important factor that contributes to the reduced thermal resistance is the increased inelastic phonon scattering at the interface and at higher temperatures. The interfacial thermal resistance computed based on the conventional acoustic mismatch model and the diffuse mismatch model is independent of temperature within the classical high temperature limit. This is because the only temperature-dependent parts for both models are the distribution functions, whereas inelastic scattering is not considered at the interfaces. The transient method applied in this work accounts for both elastic and inelastic scatterings at the interface. It has been proven that at van der Waals heterojunctions, inelastic scattering provides the major contribution to the energy transport, surpassing that of the elastic scattering at high temperatures.[25] The increase in the probability of inelastic scattering is due to the fact that, at high temperatures, the high frequency phonons might break down into large volumes of low frequency phonons. These low frequency phonons have a higher probability of getting transferred through an interface when compared to the high frequency phonons, leading to higher phonon transmission coefficients and a reduction in the overall interfacial thermal resistance for the system with increasing temperature.

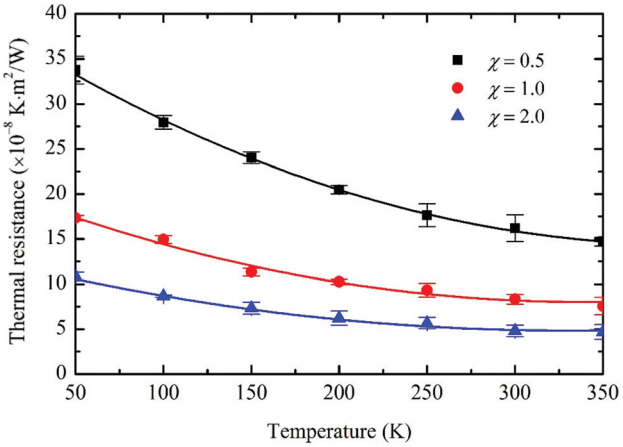

Fig. 4 Dependence of the interfacial thermal resistance on the temperature and coupling strength. The predicted R decreases monotonically with temperature and the contact pressure. Each data point is averaged over five independent simulation runs.

When the coupling strength χ increases from 0.5 to 2, the predicted thermal resistance decreases by roughly the same ratio of 70.4% at all temperature values. For example, at 300 K, R reduces from 16.2×10^{-8} K m^2 W^{-1} to 4.8×10^{-8} K m^2 W^{-1} when χ varies from 0.5 to 2. The R-decreasing trend coincides well with previous studies of SiO_2/Si [35] and silicene/SiO_2 [10] interfaces. The enhancement of thermal transport across the interface mainly comes from two aspects. First, the increase in χ enhances the contact pressure, which directly strengthens the graphene/phosphorene phonon coupling, and reduces the thermal resistance. Second, the P atoms in phosphorene act as scattering centers of graphene. The enhanced coupling strength at the interface makes graphene's intrinsic coupling between lateral and out-of-plane phonons stronger, which indirectly facilitates the thermal dissipation.

3.2 Effects of vacancy defects

The exceptional mechanical, electrical, and thermal properties of graphene can be attributed to its unique sp^2 covalent bonds between carbon atoms.[36] However, some defects are still inevitable during the fabrication of graphene sheets.[37–39] The structural defects can significantly affect the chemical, electronic and magnetic properties of graphene.[40–42] However, the effect of surface defects on interfacial thermal transport, especially for bilayer vdW structures, has not been reported in the literature.

Here, randomly distributed single-vacancy defects (inset of Fig. 5) are created on the graphene monolayer with a 0.5% to 2.5% fraction of the defects. Fig. 5 shows that the predicted thermal resistance R decreases monotonically on increasing the fraction of the defects. A 34.8% R reduction is seen when the fraction of defects increases from 0 to 2.5%. The enhanced lateral and out-of-plane phonon (ZA) coupling in graphene is the major source of interfacial thermal transport. The phonon coupling between in-plane transverse (TA) and longitudinal phonons (LA) is proven to be much faster than those between TA/LA ↔ ZA phonons. Based on the dynamic excitation theory, the phonon-coupling time between TA/LA ↔ ZA is 4.7 times longer than that between TA ↔ LA.[43] Since the kinetic energies are evenly distributed among all directions during the heating process, two thirds of the thermal energies are confined in the lateral directions after introducing the thermal impulse. The energy flow rates from the in-plane to out-of-plane phonons can be strengthened by introducing defects into the graphene monolayer, thereby promoting the reduction of interfacial thermal resistance between graphene and phosphorene. To quantitatively confirm this point, the phonon power spectra of pristine and 2.5% defect-containing graphene are computed, and the lateral/flexural PDOS are presented separately in Fig. 6. The overlap areas can be calculated as $\delta = \int \omega A(\omega) \mathrm{d}\omega$,

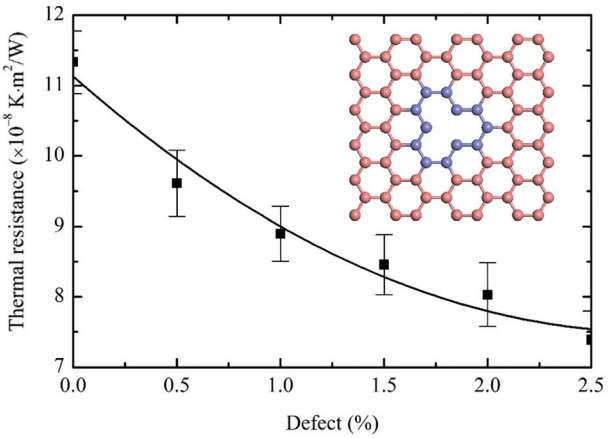

Fig. 5 Variations of thermal resistance with the fraction of defects in graphene. The calculated R decreases with the defect fraction due to the enhanced phonon coupling within the graphene monolayer. Each data point is averaged over five independent simulation runs. Pink spheres in the inset represent general carbon atoms; blue spheres denote carbon atoms around the single-vacancy defect.

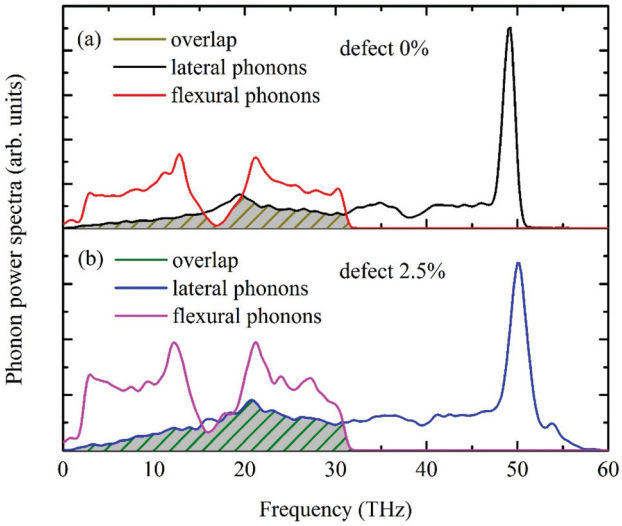

Fig. 6 Lateral and flexural phonon power spectra of graphene at (a) 0% defect and (b) 2.5% defect levels. The overlap areas become larger at a higher defect level, indicating the enhanced phonon coupling between in-plane and out-of-plane phonons in graphene.

where $A(\omega)$ represents the intersection area at frequency ω. The calculated δ for pristine graphene equals 0.348, whereas δ increases to 0.390 for 2.5% defect-containing graphene. The increased overlap areas indicate better couplings between in-plane and out-of-plane phonons in defective graphene, which indirectly enhances the interfacial thermal transport.

To further explain the decreasing trend of R on increasing the fraction of defects, phonon-power spectra for both graphene and phosphorene under different defect levels are calculated and presented in Fig. 7. The PDOS of phosphorene remain unchanged in all cases, indicating that the defects in graphene barely affect phosphorene. For graphene, the high-frequency G-band phonons exhibit a significant blue-shift on increasing the defect levels. The calculation results are consistent with previous studies.[44–46] This frequency blue-shift is an outcome of the strong anharmonic phonon–phonon coupling in MD simulations, demonstrating that the single-vacancy defect improves the energy exchange between in-plane LA/TA phonons and out-of-plane ZA phonons.

Due to the isotopic phonon power spectra in phosphorene, it can be speculated that defects in phosphorene would have less effect on the predicted interfacial thermal resistance compared to graphene. Unlike graphene, the lateral and flexural phonons in phosphorene are well mixed in the crystalline structures. To validate this presumption, additional simulations are performed with a low defect ratio of 0.5% in phosphorene at temperature 150 K. The calculation result averaged over 5 independent simulations is 11.49×10^{-8} K m^2 W^{-1}, very close to the zero-defect value of 11.33×10^{-8} K m^2 W^{-1}. However, for the same defect ratio of 0.5% in graphene, the interfacial thermal resistance is reduced to 9.61×10^{-8} K m^2 W^{-1}, about 15.2% lower than the zero-defect result.

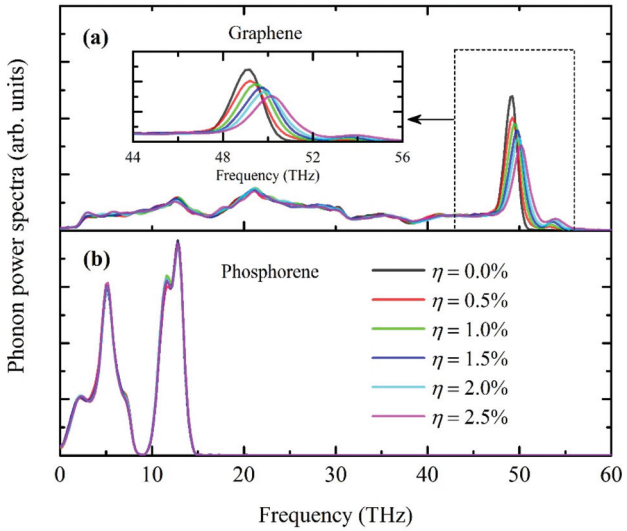

Fig. 7 Phonon-power spectra of (a) graphene and (b) phosphorene at different defect levels. The PDOS of phosphorene remains unchanged in all cases. The in-plane high frequency phonons in graphene are flattened and a significant blue-shift is observed. The integration area of each profile is normalized to unity for comparison.

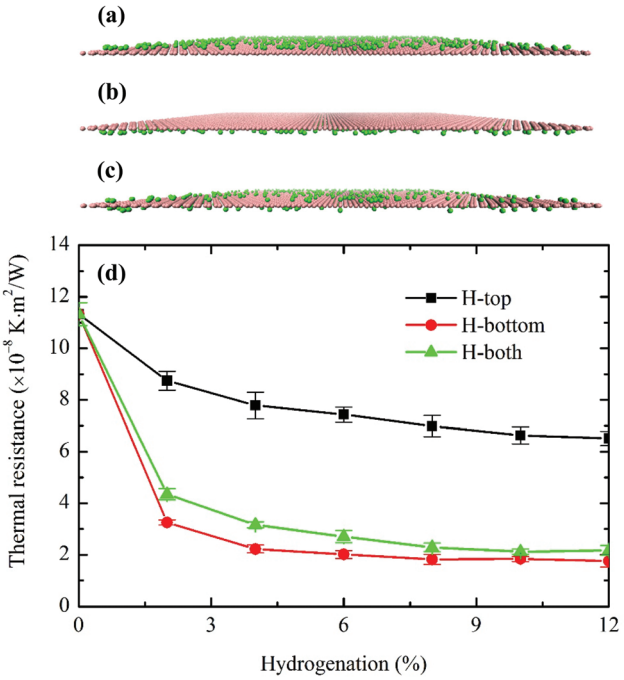

Fig. 8 Atomic configurations of (a) H-top, (b) H-bottom and (c) H-both hydrogenation types. Pink layers represent graphene; green spheres denote adsorbed hydrogen atoms. (d) Effect of hydrogenation on the interfacial thermal transport between phosphorene and graphene. The predicted R decreases monotonically with hydrogenation coverage. Each data point is averaged over five independent simulation runs.

3.3 Effects of hydrogenation

Chemical functionalization is an effective approach to modify the thermal, chemical, and mechanical properties of graphene. The fracture strain, shear modulus and shear strength of graphene can be reduced as much as 50% with the hydrogen coverage at 30%.[47] Other mechanical properties remain insensitive to hydrogen coverage. It has been found that both the concentration and configuration of hydrogen functional groups have significant influence on the thermal conductivity. By adjusting the coverage and distribution patterns of hydrogen adsorbates on graphene's edge or surface, significant thermal rectifications can be achieved.[48–50] Due to the significant effects of hydrogenation on thermal transport, it is necessary to investigate its impact on the interfacial thermal conductance between phosphorene and graphene.

In practice, hydrogen atoms can be attached to the single or both sides of a graphene sheet. Therefore, all three cases, *i.e.* H-top (graphene is between H atoms and phosphorene), H-bottom (H atoms between graphene and phosphorene) and H-both (H atoms on both sides of graphene), are considered in this work with the coverage ranging from 0% to 12%, while the pattern is random. Atomic configurations of the hydrogenated graphene monolayer are depicted in Fig. 8(a)–(c). Note that for the H-both structure, the total number of hydrogen atoms from both sides equals to those of H-top/H-bottom from one side at the same coverage ratio. As shown in Fig. 8(d), the predicted interfacial thermal resistance R decreases monotonically with the hydrogen coverage. The minimum R occurs when hydrogen atoms are added to the bottom of graphene, *i.e.*, sandwiched between graphene and phosphorene. In this case, the maximum R reduction of 84.5% is observed at 12% hydrogen coverage. When H atoms are directly in contact with P atoms in phosphorene, the phonon coupling between the two sheets is much stronger than other cases, and it offsets the enlarged distances between graphene and phosphorene. The enhanced thermal transport can be attributed to two main factors. First, the extra phonon coupling between H and P atoms directly facilitates the thermal transport at the interface. Compared to the individual graphene monolayer, an extra H–P heat dissipation channel is created in addition to that between C–P atoms. Contributions from this new heat dissipation channel can enhance the surface phonon coupling and reduce the interfacial thermal resistance. Second, the hydrogenation can be treated as surface modification to graphene, which bears similar effects as single-vacancy defect. The absorbed H atoms on graphene can also behave as scattering centers, thereby enhancing the graphene's lateral to flexural direction phonon coupling which indirectly strengthens the thermal transmission from graphene to phosphorene. The enhanced phonon couplings between graphene and phosphorene with hydrogenation can be further proven by the phonon power spectrum analyses. The H-bottom structure is selected for the PDOS computation, and the phonon power spectra of pristine graphene/phosphorene and 12% hydrogen doped graphene/phosphorene are shown in Fig. 9. It is seen that at the 12% hydrogenation level, both the PDOS of graphene and phosphorene are broadened

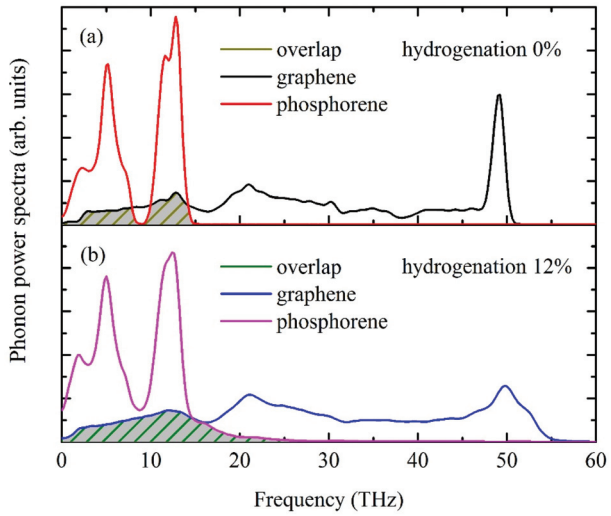

Fig. 9 Phonon power spectra of graphene and phosphorene at (a) 0% and (b) 12% hydrogenation levels. The overlap areas increase with a higher hydrogenation ratio, indicating the enhanced phonon couplings between graphene and phosphorene.

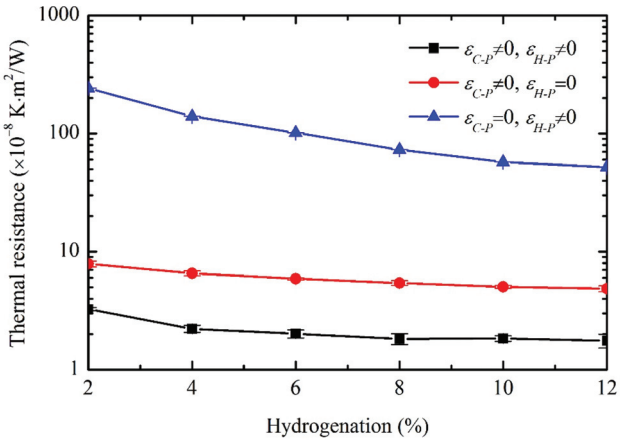

Fig. 10 A comparison of the interfacial thermal resistance with contributions from only C atoms and H atoms. The predicted R has the lowest values when both C and H atoms are involved in the thermal transport, while it has significantly higher values when only H atoms contribute to the thermal transport.

and a larger overlap is observed, indicating the enhanced phonon interactions between graphene and phosphorene.

Although the interfacial thermal resistance between graphene and phosphorene can be reduced by hydrogen functionalization, the quantitative contributions of H and C atoms to the thermal transport are still open questions. The effects of H atoms on the enhanced thermal transport can be understood by turning off the interactions between C–P atoms or H–P atoms. Since minimum R occurs when H atoms reside in the middle of graphene and phosphorene, the H-bottom configuration is used in the following calculations. The LJ parameters ε_{C-P} and ε_{H-P} are set to zero separately; the calculated R values are summarized in Fig. 10. R reaches the lowest level when both C and H atoms are involved ($\varepsilon_{C-P} \neq 0$, $\varepsilon_{H-P} \neq 0$) in the thermal transport. When only H atoms are involved ($\varepsilon_{C-P} = 0$, $\varepsilon_{H-P} \neq 0$), R increases significantly by two orders of magnitude. R values with only C atoms involved ($\varepsilon_{C-P} \neq 0$, $\varepsilon_{H-P} = 0$) are in between the two cases. The calculation results indicate that the thermal transport is still dominated by C–P interactions even with the hydrogenation. Interfacial thermal resistance is mostly dependent on the materials' atomic mass ratio at the interface. The predicted R value increases monotonically with the atomic mass ratio, which further explains the greater contributions from carbon atoms since the P/H mass ratio is 12 times higher than that of P/C.[51]

4. Conclusion

Inter-plane thermal conductance at the phosphorene–graphene vdW interface is investigated using classical MD simulations. Several modulators such as system temperature, contact pressure, vacancy defect, and hydrogenation are explored, with which significant thermal resistance reductions are observed. The maximum R reduction is predicted as 84.5% when the hydrogenation is applied on the near-phosphorene-side graphene surface. Other factors such as temperature, coupling strength, and fraction of single-vacancy defects have relatively weaker influences on R, which decrease R values by 56.5%, 70.4%, and 34.8%, respectively. The PDOS mismatch in graphene and phosphorene appears to be the key factor for the thermal resistance. Note that unlike graphene, the PDOS of phosphorene are isotropic in all directions and only exist in the low-frequency region. Reductions of R at the interface can be attributed to several factors, including increased phonon population, enhanced anharmonic phonon scattering at higher temperatures, as well as strengthened coupling between lateral and out-of-plane phonons of graphene with increasing fraction of the defect or functionalization. Note also that the interfacial thermal resistance between phosphorene–graphene is less than that of other 2D bilayer heterostructures, a distinct advantage for practical applications. Our study provides new insights into thermal resistance in the phosphorene–graphene bilayer, which can be useful for the better design of heterostructures for nanoelectronic applications.

Acknowledgements

Support from the Nebraska Center for Energy Sciences Research and the Holland Computing Center at the University of Nebraska-Lincoln is greatly appreciated.

References

1 J. Zhang, F. Xu, Y. Hong, Q. Xiong and J. Pan, *RSC Adv.*, 2015, **5**, 89415–89426.
2 J. Zhang, X. Wang and H. Xie, *Phys. Lett. A*, 2013, **377**, 2970–2978.

3 J. Zhang, X. Huang, Y. Yue, J. Wang and X. Wang, *Phys. Rev. B: Condens. Matter*, 2011, **84**, 235416.
4 S. Ghosh, I. Calizo, D. Teweldebrhan, E. P. Pokatilov, D. L. Nika, A. A. Balandin, W. Bao, F. Miao and C. N. Lau, *Appl. Phys. Lett.*, 2008, **92**, 151911.
5 M. Y. Liao and Y. Koide, *Crit. Rev. Solid State Sci.*, 2011, **36**, 66–101.
6 T. Shimizu, J. Haruyama, D. C. Marcano, D. V. Kosinkin, J. M. Tour, K. Hirose and K. Suenaga, *Nat. Nanotechnol.*, 2011, **6**, 45–50.
7 S. J. Zhang, S. S. Lin, X. Q. Li, X. Y. Liu, H. A. Wu, W. L. Xu, P. Wang, Z. Q. Wu, H. K. Zhong and Z. J. Xu, *Nanoscale*, 2016, **8**, 226–232.
8 S. J. Han, K. A. Jenkins, A. V. Garcia, A. D. Franklin, A. A. Bol and W. Haensch, *Nano Lett.*, 2011, **11**, 3690–3693.
9 J. Qiao, X. Kong, Z.-X. Hu, F. Yang and W. Ji, *Nat. Commun.*, 2014, **5**, 4475.
10 (*a*) Y. Hong, J. Zhang, X. Huang and X. C. Zeng, *Nanoscale*, 2015, **7**, 18716–18724; (*b*) Y. Hong, J. Zhang and X. C. Zeng, *J. Phys. Chem. C*, 2016, DOI: 10.1021/acs.jpcc.6b07262.
11 J. Dai and X. C. Zeng, *RSC Adv.*, 2014, **4**, 48017–48021.
12 H. Guo, N. Lu, J. Dai, X. Wu and X. C. Zeng, *J. Phys. Chem. C*, 2014, **118**, 14051–14059.
13 L. Li, Y. Yu, G. J. Ye, Q. Ge, X. Ou, H. Wu, D. Feng, X. H. Chen and Y. Zhang, *Nat Nanotechnol.*, 2014, **9**, 372–377.
14 K. S. Novoselov, A. Mishchenko, A. Carvalho and A. H. Castro Neto, *Science*, 2016, **353**, aac9439.
15 J. E. Padilha, A. Fazzio and A. J. R. da Silva, *Phys. Rev. Lett.*, 2015, **114**, 066803.
16 A. Hashmi, U. Farooq and J. Hong, *Curr. Appl. Phys.*, 2016, **16**, 318–323.
17 Y. Cai, G. Zhang and Y.-W. Zhang, *winword*, 2015, **119**, 13929–13936.
18 S. Plimpton, *J. Comput. Phys.*, 1995, **117**, 1–19.
19 W. B. Donald, A. S. Olga, A. H. Judith, J. S. Steven, N. Boris and B. S. Susan, *J. Phys.: Condens. Matter*, 2002, **14**, 783.
20 J. Jin-Wu, *Nanotechnology*, 2015, **26**, 315706.
21 M. Daniel, H. L. Caio and C. Alexander, *2D Mater.*, 2016, **3**, 011005.
22 C. Kun, W. Jing, W. Ning, C. Haifang and Q. Qing-Hua, *Nanotechnology*, 2016, **27**, 235703.
23 L. Xiangbiao, H. Feng, X. Hang and C. Xi, *Nanotechnology*, 2016, **27**, 215701.
24 A. K. Rappe, C. J. Casewit, K. S. Colwell, W. A. Goddard and W. M. Skiff, *J. Am. Chem. Soc.*, 1992, **114**, 10024–10035.
25 R. J. Stevens, L. V. Zhigilei and P. M. Norris, *Int. J. Heat Mass Tranfer.*, 2007, **50**, 3977–3989.
26 S. Yu, S. Yang and M. Cho, *J. Appl. Phys.*, 2011, **110**, 124302.
27 K. Gordiz and A. Henry, *New J. Phys.*, 2015, **17**, 103002.
28 P. E. Hopkins and P. M. Norris, *Appl. Phys. Lett.*, 2006, **89**, 131909.
29 J. Zhang, Y. Wang and X. Wang, *Nanoscale*, 2013, **5**, 11598–11603.
30 Y. Hong, L. Li, X. C. Zeng and J. Zhang, *Nanoscale*, 2015, **7**, 6286–6294.
31 X. Zhiping and J. B. Markus, *J. Phys.: Condens. Matter*, 2012, **24**, 475305.
32 B. Liu, J. A. Baimova, C. D. Reddy, A. W.-K. Law, S. V. Dmitriev, H. Wu and K. Zhou, *ACS Appl. Mater. Interfaces*, 2014, **6**, 18180–18188.
33 B. Liu, F. Meng, C. D. Reddy, J. A. Baimova, N. Srikanth, S. V. Dmitriev and K. Zhou, *RSC Adv.*, 2015, **5**, 29193–29200.
34 J. Zhang, Y. Hong and Y. Yue, *J. Appl. Phys.*, 2015, **117**, 134307.
35 J. Chen, G. Zhang and B. Li, *J. Appl. Phys.*, 2012, **112**, 064319.
36 A. K. Geim and K. S. Novoselov, *Nat. Mater.*, 2007, **6**, 183–191.
37 A. M. Dimiev, G. Ceriotti, A. Metzger, N. D. Kim and J. M. Tour, *ACS Nano*, 2016, **10**, 274–279.
38 J. S. Lee, S. I. Kim, J. C. Yoon and J. H. Jang, *ACS Nano*, 2013, **7**, 6047–6055.
39 J. H. Lee, D. W. Shin, V. G. Makotchenko, A. S. Nazarov, V. E. Fedorov, Y. H. Kim, J. Y. Choi, J. M. Kim and J. B. Yoo, *Adv. Mater.*, 2009, **21**, 4383–4387.
40 D. W. Boukhvalov and M. I. Katsnelson, *Nano Lett.*, 2008, **8**, 4373–4379.
41 G. M. Rutter, J. N. Crain, N. P. Guisinger, T. Li, P. N. First and J. A. Stroscio, *Science*, 2007, **317**, 219–222.
42 M. Sepioni, R. R. Nair, S. Rablen, J. Narayanan, F. Tuna, R. Winpenny, A. K. Geim and I. V. Grigorieva, *Phys. Rev. Lett.*, 2010, **105**, 207205.
43 J. Zhang, X. Wang and H. Xie, *Phys. Lett. A*, 2013, **377**, 721–726.
44 D. Liu, P. Yang, X. Yuan, J. Guo and N. Liao, *Phys. Lett. A*, 2015, **379**, 810–814.
45 Y. L. Yang and Y. Lu, *Chin. Phys. B*, 2014, **23**, 106501.
46 P. Anees, M. C. Valsakumar and B. K. Panigrahi, *2D Mater.*, 2015, **2**, 035014.
47 A. Hadizadeh Kheirkhah, E. Saeivar Iranizad, M. Raeisi and A. Rajabpour, *Solid State Commun.*, 2014, **177**, 98–102.
48 H. Fan, L. Deng, X. Yuan, J. Guo, X. Li and P. Yang, *RSC Adv.*, 2015, **5**, 38001–38005.
49 Y. Tang, J. Li, X. Wu, Q. Liu, Y. Liu and P. Yang, *Appl. Surf. Sci.*, 2016, **362**, 86–92.
50 C. Melis, G. Barbarino and L. Colombo, *Phys. Rev. B: Condens. Matter*, 2015, **92**, 245408.
51 S. Wang and X. Liang, *Int. J. Thermophys.*, 2010, **31**, 1935–1944.
52 M. Li, J. Zhang, X. Hu and Y. Yue, *Appl. Phys. A: Mater. Sci. Process.*, 2015, **119**, 415–424.
53 H. Wang, J. Gong, Y. Pei and Z. Xu, *ACS Appl. Mater. Interfaces*, 2013, **5**, 2599–2603.
54 S.-W. Chang, A. Nair and M. Buehler, *J. Phys.: Condens. Matter*, 2012, **24**, 245301.
55 T. Luo and J. R. Lloyd, *Adv. Funct. Mater.*, 2012, **22**, 2495–2502.
56 J. Park and V. Prakash, *J. Appl. Phys.*, 2014, **116**, 014303.
57 Z. Wei, Z. Ni, K. Bi, M. Chen and Y. Chen, *Phys. Lett. A*, 2011, **375**, 1195–1199.
58 J. Zhang, Y. Hong, Z. Tong, Z. Xiao, H. Bao and Y. Yue, *Phys. Chem. Chem. Phys.*, 2015, **17**, 23704–23710.